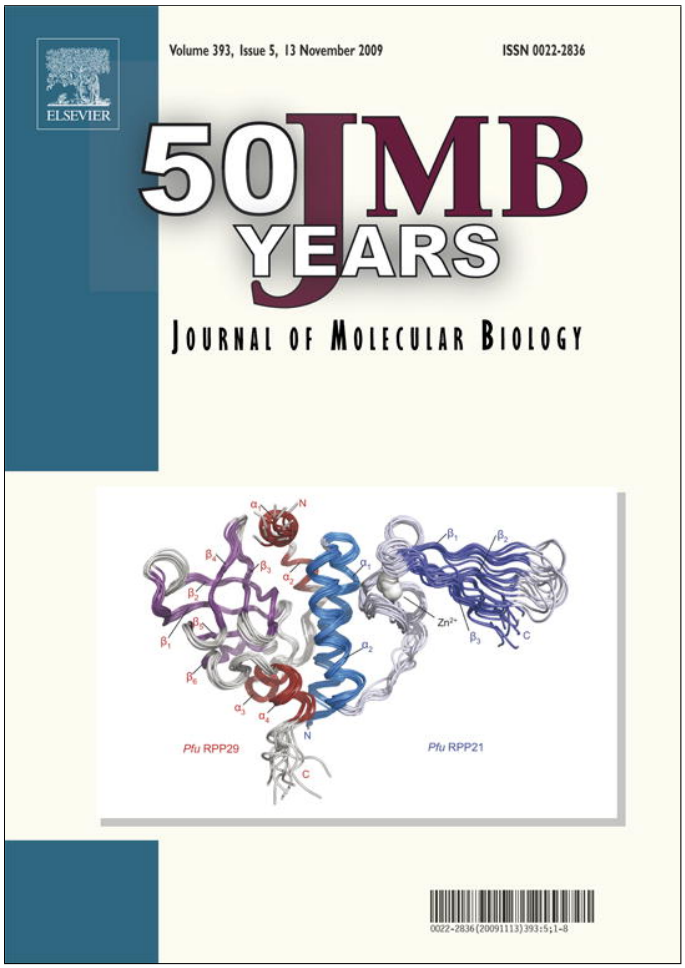

doi:10.1016/j.jmb.2009.08.068 J. Mol. Biol. (2009) 393, 1043–1055

JMB

Available online at www.sciencedirect.com

ScienceDirect

ELSEVIER

Solution Structure of an Archaeal RNase P Binary Protein Complex: Formation of the 30-kDa Complex between *Pyrococcus furiosus* RPP21 and RPP29 Is Accompanied by Coupled Protein Folding and Highlights Critical Features for Protein–Protein and Protein–RNA Interactions

Yiren Xu[1,2], Carlos D. Amero[2,3]†, Dileep K. Pulukkunat[1,2]†, Venkat Gopalan[1,2,3]* and Mark P. Foster[1,2,3]*

[1]*Ohio State Biochemistry Program, Center for RNA Biology, The Ohio State University, Columbus, OH 43210, USA*

[2]*Department of Biochemistry, Center for RNA Biology, The Ohio State University, Columbus, OH 43210, USA*

[3]*Biophysics Graduate Program, Center for RNA Biology, The Ohio State University, Columbus, OH 43210, USA*

Received 30 July 2009; received in revised form 28 August 2009; accepted 30 August 2009
Available online 3 September 2009

Edited by M. F. Summers

Ribonuclease P (RNase P) is a ribonucleoprotein (RNP) enzyme that catalyzes the Mg^{2+}-dependent 5′ maturation of precursor tRNAs. In all domains of life, it is a ribozyme: the RNase P RNA (RPR) component has been demonstrated to be responsible for catalysis. However, the number of RNase P protein subunits (RPPs) varies from 1 in bacteria to 9 or 10 in eukarya. The archaeal RPR is associated with at least 4 RPPs, which function in pairs (RPP21–RPP29 and RPP30–POP5). We used solution NMR spectroscopy to determine the three-dimensional structure of the protein–protein complex comprising *Pyrococcus furiosus* RPP21 and RPP29. We found that the protein–protein interaction is characterized by coupled folding of secondary structural elements that participate in interface formation. In addition to detailing the intermolecular contacts that stabilize this 30-kDa binary complex, the structure identifies surfaces rich in conserved basic residues likely vital for recognition of the RPR and/or precursor tRNA. Furthermore, enzymatic footprinting experiments allowed us to localize the RPP21–RPP29 complex to the specificity domain of the RPR. These findings provide valuable new insights into mechanisms of RNP assembly and serve as important steps towards a three-dimensional model of this ancient RNP enzyme.

Keywords: ribonuclease P, RNase P; archaea; NMR of a protein-protein complex; binding-coupled protein folding; RNA footprinting

**Corresponding authors.* E-mail addresses: gopalan.5@osu.edu; foster.281@osu.edu.

† C.D.A. and D.K.P. contributed equally to this work.

Present addresses: C. D. Amero, Institut de Biologie Structurale, CNRS, Grenoble, France; D. K. Pulukkunat, Department of Chemistry, Columbia University, New York, NY, USA.

Abbreviations used: RNP, ribonucleoprotein (RNA + protein); RNase P, ribonuclease P; RPP, RNase P protein subunit; RPR, RNase P RNA subunit; *Pfu*, *Pyrococcus furiosus*; *Mja*, *Methanocaldococcus jannaschii*; NOE, nuclear Overhauser effect; *Pho*, *Pyrococcus horikoshii*; HSQC, heteronuclear single quantum coherence; *Mth*, *Methanothermobacter thermautotrophicus*; CSP, chemical shift perturbation; 3D, three-dimensional; NOESY, nuclear Overhauser effect spectroscopy; TSL, T stem–loop.

Introduction

Ribonuclease P (RNase P), a ribonucleoprotein (RNP) complex, catalyzes removal of the 5′ leader sequence during tRNA maturation.[1–3] Across the three domains of life, it is composed of one RNA subunit and a varying number of protein subunits: one in bacteria, at least four in archaea, and nine in eukarya. The RNase P RNA (RPR) from each domain of life has been shown to be catalytic on its own *in vitro* under elevated monovalent and divalent ion concentrations.[4–6] However, RNase P protein(s) (RPPs) enhance catalysis under near-physiological conditions by facilitating RPR folding, substrate recognition, and decrease in the

Mg^{2+} requirement.[7–10] Interestingly, when the enzyme from the three domains of life is compared, an increase in protein content is associated with the loss of some RPR elements and a concomitant decrease in RPR activity.[1,4,11,12] Thus, RNase P is an appealing model to address how protein cofactors might have taken over the structural and functional attributes of RNAs during evolution from a putative RNA-centric world to the present protein-centric one. Towards the goal of understanding this progression, we have focused our efforts on the biochemically tractable and thermostable archaeal version of the RNase P enzyme from the hyperthermophilic archaeon *Pyrococcus furiosus* (*Pfu*), whose RPPs are homologous to their eukaryal counterparts.[13,14]

Bacterial RNase P is the best understood form of the enzyme.[15] Based on the primary sequence and secondary structure of the RPRs, bacterial RNase P can be classified into two distinct types: A and B.[16] In both types, the RPR is composed of two independently folding domains, termed the specificity and catalytic domains (S domain and C domain, respectively), held together by interdomain RNA–RNA contacts.[17] To date, crystallographic structures have been reported for two S domains and two full-length RPRs, from bacterial RNase P of types A and B.[18–21] The structures of three homologous bacterial RPPs have been solved by crystallography or NMR spectroscopy as well.[22–24] Although the structure of the bacterial RNase P holoenzyme complex has not yet been determined, models of A- and B-type RNPs have been built using a wealth of information from biochemical studies.[25–27]

Phylogenetic and biochemical studies have revealed that archaeal RNase P is a compositional intermediate between the bacterial and eukaryotic counterparts. Euryarchaeal RNase P can also be categorized into two groups based on their RPR sequences: A and M.[16,28] Euryarchaeal A-type RPR (e.g., *Pfu*) is similar to the bacterial A-type in terms of secondary structures and reported *in vitro* catalytic activity;[5,13] in contrast, the M-type RPR more closely resembles the eukaryotic RPR and has shown no catalytic activity on its own, although it can cleave a substrate tethered in cis.[29] Though no high-resolution structure of the archaeal RPR is available, secondary-structure similarities and the presence of universally conserved nucleotides in the active site suggest that the archaeal RPR fold (especially the C domain) might resemble that of the bacterial RPR; however, the increased RPP content in archaeal RNase P suggests that RNA–protein interactions in the enzyme are likely to have replaced some of the intramolecular RNA–RNA interactions present in the bacterial RPR.[12]

Although the archaeal and eukaryotic RPRs share conserved structural features with their bacterial counterparts, none of the RPPs from archaeal or eukaryotic RNase P share sequence similarity with the single bacterial protein. At least four protein subunits are associated with *Pfu* RNase P and share sequence homology to the human RPPs: RPP21, RPP29, RPP30, and POP5.[14] The structures of the four archaeal RPPs have been solved from different archaeal organisms by either NMR spectroscopy or X-ray crystallography, or both. These studies on the isolated proteins revealed the structures of the RPPs to fall within common nucleic acid binding protein families: an Sm-like fold (RPP29),[30–33] a zinc ribbon (RPP21),[34,35] an RRM-like fold (Pop5),[36] and a TIM barrel (RPP30).[37]

Biochemical data have suggested that at least some of the archaeal and eukaryotic RPPs function in pairs. Yeast two-hybrid studies of proteins from both archaeal and eukaryotic RNase P confirmed the presence of two binary complexes: RPP21–RPP29 and RPP30–POP5.[38–40] Reconstitution assays performed on *Pfu* RNase P have shown that either protein pair is sufficient to activate the RNA enzyme at lower ion concentrations, while no single protein can rescue the RNA enzyme under the same conditions.[13] Although these studies established a role for RPP binary pairs in enhancing the catalytic activity of archaeal RPRs, the mechanistic basis for their actions is largely unclear without useful structural models of the archaeal RNase P holoenzyme. To that end, high-resolution structure determination of the binary complexes is a necessity.

Here, we report the NMR-derived solution structure of the 30-kDa complex between two *Pfu* RPPs: the Sm-like RPP29 and the zinc-ribbon RPP21 proteins. This study complements recently reported crystal structures of the *Pyrococcus horikoshii* (*Pho*) POP5–RPP30 and RPP21–RPP29 complexes,[41,42] reveals dynamic features of the proteins and binding-coupled protein folding events, and identifies additional features important for protein–protein and protein–RNA interactions. Furthermore, footprinting studies allow us to map the RPP21–RPP29 complex onto the S domain of the RPR. Together with biochemical studies on the C domain and RPP30–POP5 complex from *Pfu* and *Methanocaldococcus jannaschii* (*Mja*),[13,29] this work represents an important step towards understanding the architecture and function of archaeal and eukaryal RNase P.

Results and Discussion

NMR spectroscopy of the RPP29–RPP21 complex

At lower temperatures (25 and 40 °C), NMR spectra of free *Pfu* RPP21 and RPP29 were of poor quality, with broad lines and highly variable peak intensities, suggesting that the proteins were poorly folded and/or aggregated at those temperatures. Spectra recorded at 55 °C yielded generally narrow lines and uniform peak intensities for both proteins, and thus, data were recorded at 55 °C for both the free proteins and the protein–protein complexes. The ^{15}N-edited heteronuclear single quantum coherence (HSQC) spectrum of free *Pfu* RPP29

contains only 62 of 124 expected backbone resonances (Supporting Information), suggesting that only its Sm-like core is folded in solution in the monomer state. This observation is consistent with the previously reported solution structures of RPP29 from *Archaeoglobus fulgidus*[31] and *Methanothermobacter thermautotrophicus* (*Mth*).[30] In free RPP21, 78 backbone amides could be assigned in the free protein, revealing a structured core comprising residues 19 to 105, out of a total of 123.[35] As unlabeled RPP21 is titrated into ^{15}N-labeled RPP29, signals from free RPP29 disappear, with concomitant appearance of a new set of resonances corresponding to RPP21-bound RPP29, until the samples

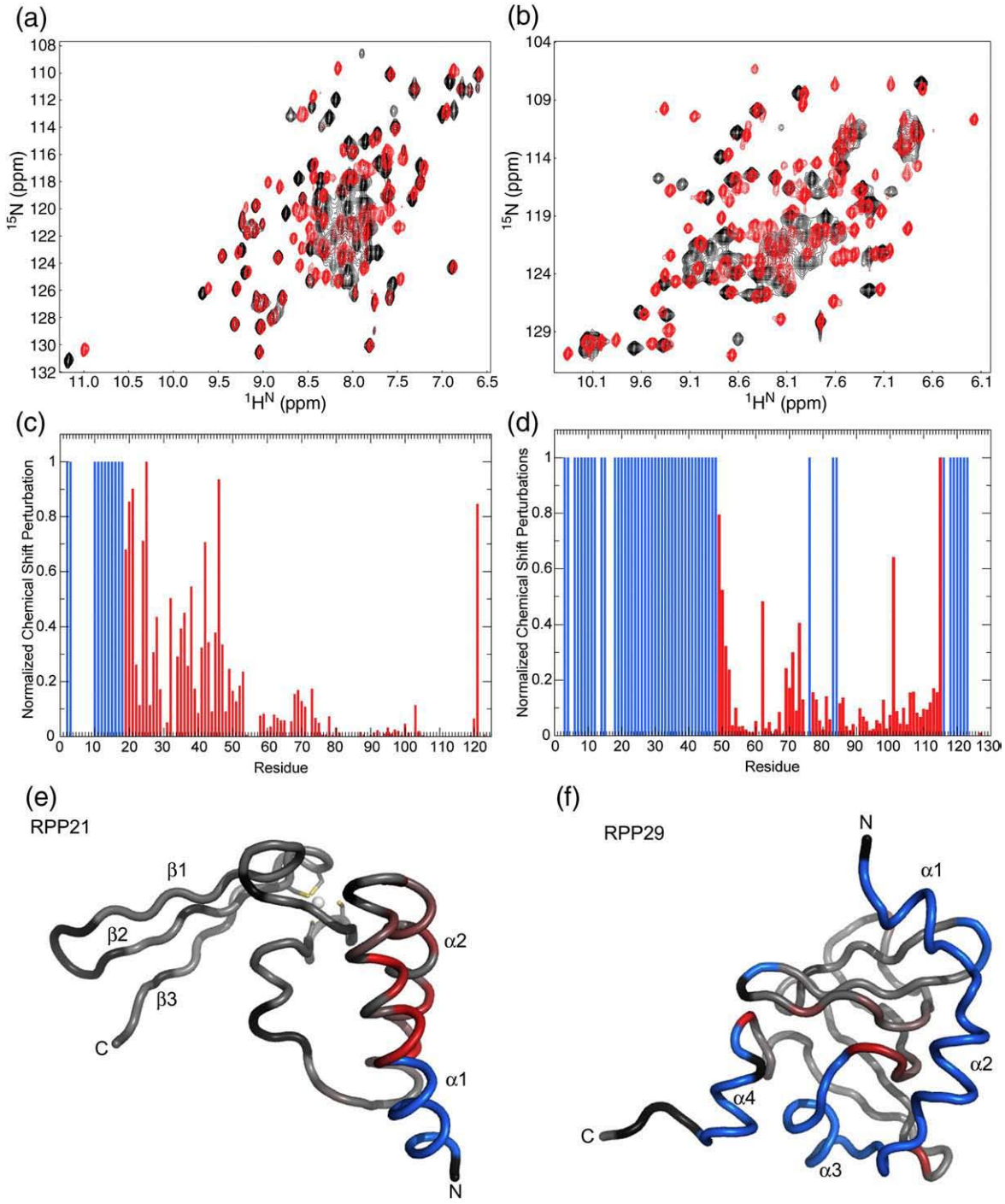

Fig. 1. Binding-coupled folding in *Pfu* RPP21 and RPP29 as detected by NMR. Overlay of ^{15}N HSQC spectra of each ^{15}N-labeled protein in the absence (black) and presence (red) of its partner illustrates the site-specific CSPs. Weighted average CSP values (c and d) are mapped onto cartoon diagrams of the proteins (e, RPP21 and f, RPP29) using a linear color ramp from gray (no change) to red (maximal CSP). Blue indicates residues whose signals were only observed in the spectra of the complex. Black, undetermined CSP.

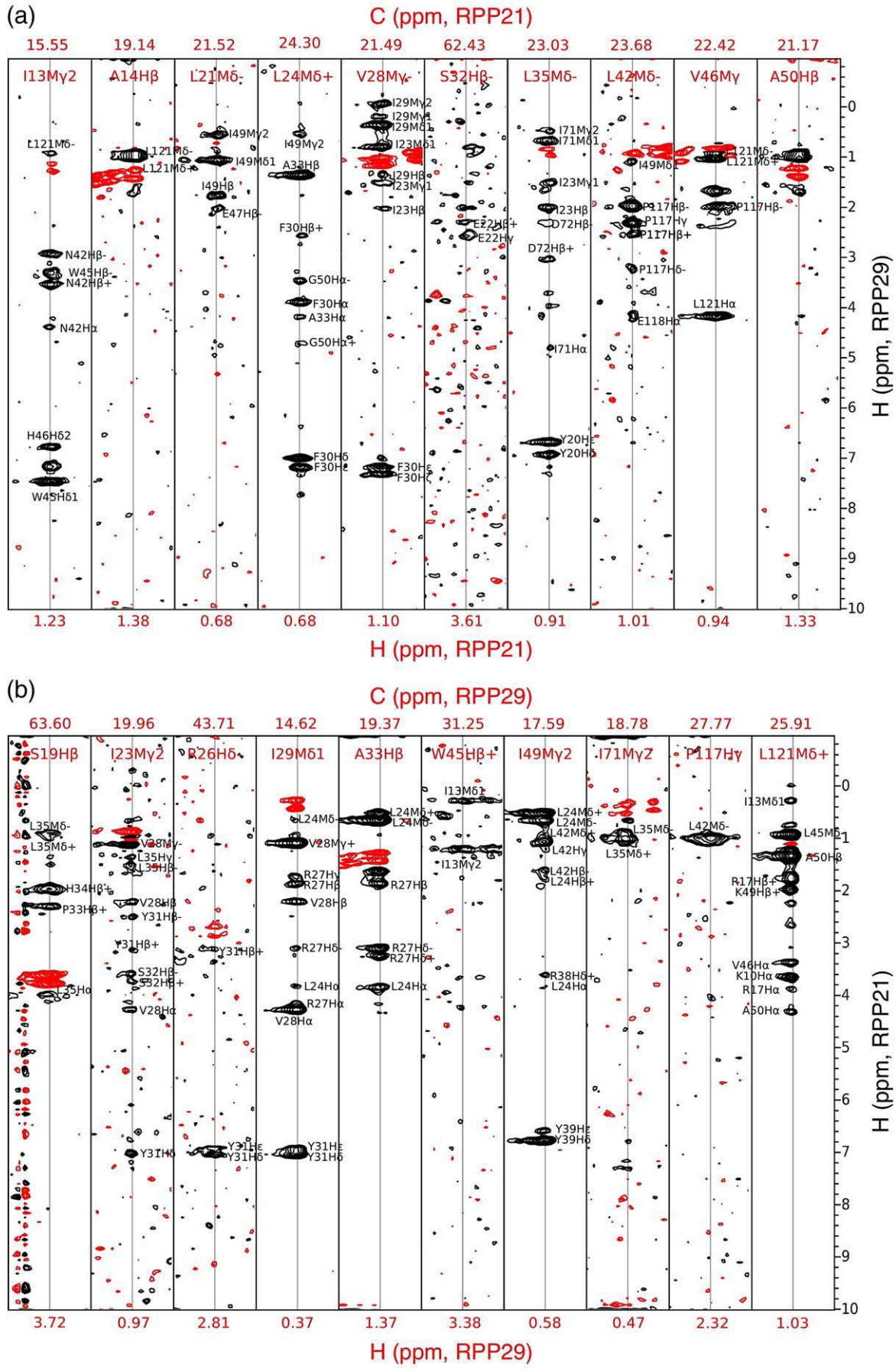

Fig. 2 (*legend on next page*)

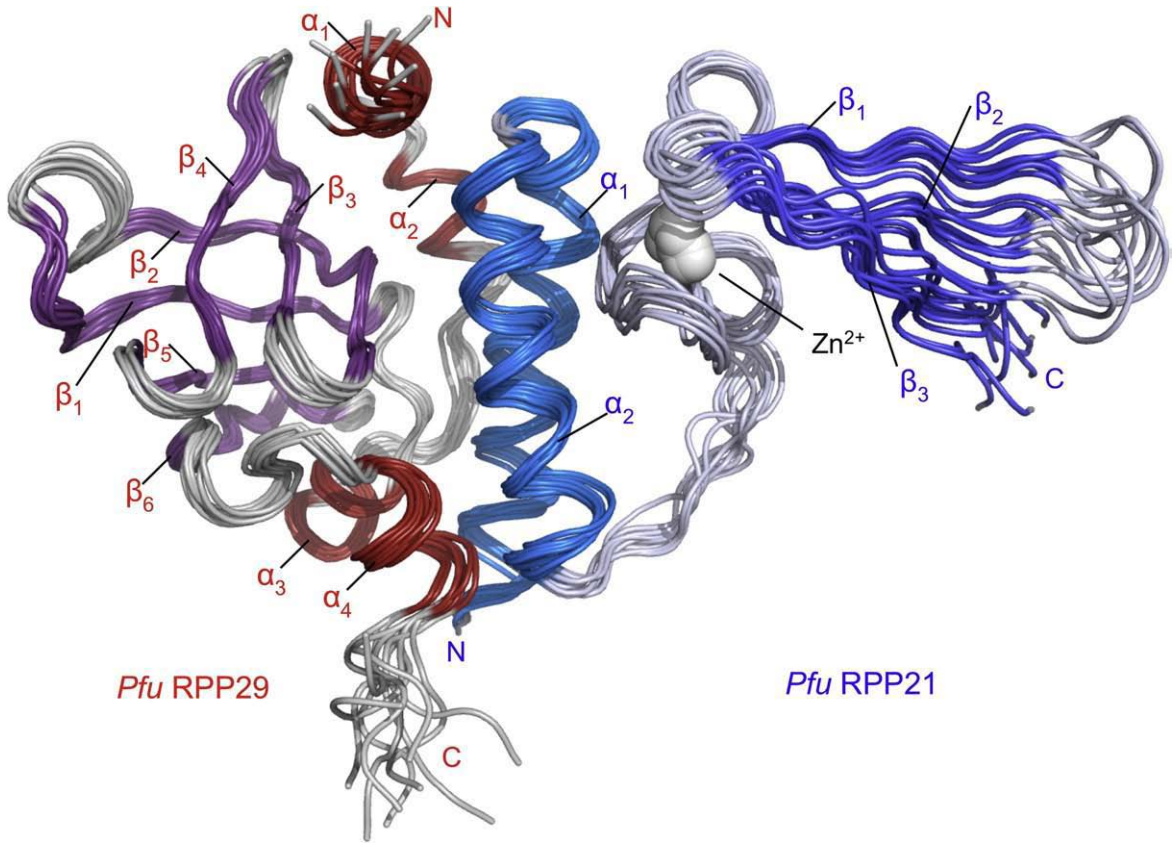

Fig. 3. Solution structure of the *Pfu* RPP29–RPP21 complex. Ensemble of 10 lowest-energy structures superimposed on the backbone heavy atoms of residues 18–122 of RPP29 and residues 10–54, 57–81, and 88–104 of RPP21. *Pfu* RPP29 and RPP21 are labeled in red and blue, respectively.

reach a molar ratio of 1:1 of RPP29 and RPP21, beyond which no further change in the spectrum is observed. This behavior corresponds to the slow exchange regime for the equilibrium between the free and bound states and is indicative of tight binding and a 1:1 stoichiometry.

Strikingly, 52 new RPP29 backbone amide resonances are observed in ^{15}N-edited spectra of the RPP21-bound RPP29. This number corresponds overall to 42% of the RPP29 primary sequence and accounts for nearly all of the resonances that were not observed in spectra of the free protein. Among these 52 new signals, 41 arise from residues at the N-terminus and 8 from the C-terminus, implying that the termini, which are disordered in free RPP29, fold upon binding to RPP21 and play an important role in forming the RPP21 binding interface (Fig. 1 and Supporting Information).

Spectra of bound RPP21 also revealed signals not observed in the free protein. Upon binding to unlabeled RPP29, nine new backbone amide resonances could be assigned to residues from the N-terminal helical bundle of the protein. In addition, the amides that exhibited the largest chemical shift perturbations (CSPs) upon binding RPP29 are primarily from residues clustered at the N-terminal helical bundle of RPP21, including D19, I20, L21, L24, A25, R27, V28, S32, R38, L42, and V46 (Fig. 1 and Supporting Information). These data highlight the RPP29 binding region of RPP21[35] and indicate that the interaction with RPP29 stabilizes the secondary structure in this region of RPP21.

Mutations in the unstructured helical bundle of free RPP21 are deleterious to RPP29 binding. We initially used an RPP21 Ala14Val variant (denoted RPP21V14) in our structural studies due to inadvertent selection of a clone with this spurious mutation. The ^{1}H–^{15}N correlated spectra of RPP21V14[35] and of the wild-type protein are nearly identical, indicating that the N-terminal region containing this residue is unstructured in both proteins (data not shown), although helix α_1 was observed to extend through this region in crystallographic studies of *Pho* RPP21.[34] Ala14 in RPP21 is highly conserved through archaea and eukarya (Supporting Information), suggesting that the residue may play an

Fig. 2. Representative strips from ^{13}C-filtered/edited NOE spectra recorded on (a) [U-^{13}C,^{15}N]RPP21 bound to unlabeled *Pfu* RPP29 and (b) [U-^{13}C,^{15}N]RPP29 with unlabeled RPP21. The black (positive) cross peaks arise from intermolecular NOEs, while the red (negative) peaks result from incomplete suppression of self- and intramolecular NOEs. The ^{1}H and ^{13}C shifts of the labeled partner are indicated above and below each strip, while the *y*-axis corresponds to the shift of ^{1}Hs from the unlabeled partner to which the labeled proton NOEs.

important role in maintaining overall structural integrity or interaction with its partner RPP29. Notably, we found that wild-type RPP21 binds to RPP29 3-fold tighter than the mutant (not shown), and no new amide signals appeared when [U-^{15}N] RPP21V14 is saturated with RPP29, in contrast to the nine new N-terminal resonances observed when wild-type RPP21 binds its partner. This implies that similar to RPP29, RPP21 experiences binding-coupled folding and that an A14V mutation in RPP21 interferes with this aspect of the interaction.

CSPs allowed preliminary identification of the binding interface between RPP29 and RPP21. Detailed characterization of the binding interface was achieved by recording and assigning intermolecular nuclear Overhauser effects (NOEs), which were obtained from three-dimensional (3D) ^{13}C-filtered/edited NOE spectroscopy (NOESY) spectra recorded in 99.8% D_2O.[43,44] Cross peaks in these spectra arise from NOEs between protons not attached to ^{13}C nuclei (the filter step) to protons attached to ^{13}C nuclei (the editing step), thereby providing exclusively intermolecular NOEs when one of the proteins is uniformly ^{13}C labeled and the other is unlabeled. We recorded ^{13}C-filtered/edited NOESY spectra on both [U-^{13}C,^{15}N]RPP29 in complex with unlabeled RPP21 and on [U-^{13}C,^{15}N] RPP21 in complex with unlabeled RPP29 (Fig. 2). These spectra yielded a total of 284 intermolecular NOEs (153 and 131 NOEs from each spectrum; Supporting Information).

Table 1. Structural statistics for the RPP29–RPP21 complex

	RPP29	RPP21
NMR constrains		
NOEs	2038	1407
Intraresidue ($i-j=0$)	833	606
Sequential ($i-j=1$)	475	364
Short range ($1<i-j<5$)	204	203
Long range ($i-j>5$)	526	234
Intermolecular (RPP29−RPP21)	472	
Ambiguous	376	328
Hydrogen bonds[a]	38	80
Dihedral angles	188	162
Structure statistics		
Violations		
Distance violations >0.5 Å	1.50±1.02	
Dihedral angle violations >5°	1.63±0.10	
Deviation from idealized geometry		
Bonds (Å)	0.0046±0.00008	
Angles (°)	0.77±0.02	
Impropers (°)	0.56±0.01	
Ramachandran statistics (%)[b]		
Favored	77.0	
Additionally allowed	21.1	
Generously allowed	1.4	
Disallowed	0.5	
Precision (RMSD form the mean structure)[c]		
Backbone atoms (Å)	0.58	
All heavy atoms (Å)	0.87	

[a] Hydrogen bonds were applied as upper-bound restraints between amide proton and oxygen atoms and between amide nitrogen and oxygen atoms.
[b] Ramachandran analysis was performed using PROCHECK-NMR.[45]
[c] Structure statistics were calculated using the 10 lowest-energy structures; RMSDs were calculated by superimposing residues 18–122 of RPP29 and residues 9–54, 57–81, and 86–104 of RPP21.

Solution structure of the *Pfu* RPP29–RPP21 complex

The solution structure of the *Pfu* RPP29–RPP21 complex (Fig. 3) was determined by iterative torsion-angle refinement using distance restraints derived from inter- and intramolecular NOEs, hydrogen-bond restraints inferred from secondary-structure information, and torsion-angle restraints from analysis of chemical shifts. The ensemble is well defined for the assigned residues (17–123 of RPP29 and 9–54, 57–81, and 86–104 of RPP21) with a mean root-mean-square deviation (RMSD) of 0.58 and 0.87 Å for backbone and heavy atoms, respectively. The stereochemical quality of the structures was high, with 98.1% of the residues adopting φ and ψ angles falling in the most favored and the additionally favored regions of the Ramachandran plot (Table 1). The extreme N- and C-termini of both proteins (residues 1–16 and 124–127 of RPP29; residues 1–8 and 105–123 of RPP21) are flexible in the complex, as confirmed by {^{1}H}–^{15}N heteronuclear NOE data (Supporting Information), indicating that these regions are not involved in the interaction with the protein partner.

In the RPP29–RPP21 complex, additional structural elements from each protein could be resolved, which were disordered in their free proteins. For RPP29, in addition to the signals from the β-barrel core, binding RPP21 allowed definition of residues from three helices (helix α_1, residues 19–23; helix α_2, residues 27–31; and helix 3, residues 40–44), an extended strand connecting helix α_2 and helix α_3 at the N-terminus, and a C-terminal helix (helix α_4, residues 117–122). In the context of the RPP21 complex, the packing of several N-terminal residues of RPP29 within the Sm-like core of the protein (I24, T27, R31, H34, V38, K40, and L44) is stabilized, although these intramolecular interactions were insufficient to stabilize the interactions in the free protein. In contrast to the extensive intramolecular contacts made by the binding-stabilized N-terminal residues, the RPP29 C-terminal helix observed in the complex appears to be entirely stabilized by intermolecular contacts to RPP21, as few intramolecular NOEs are observed from this region of the protein to other parts of RPP29. The Sm-like core of RPP29 is essentially unchanged by RPP21 binding as the RMSD between the free and RPP21-bound structures is within the precision of the ensemble (~1.1 Å for backbone atoms). Thus, it is evident that binding of RPP29 to RPP21 involves binding-coupled folding and stabilization of interfacial structures in RPP29.

When bound to its partner, RPP21 adopts the same overall L-shaped structure observed in the free protein: a long arm containing the two N-terminal α-helices, a short-arm made up of the C-terminal β-sheet comprising the zinc ribbon, and a

central linker connecting the two domains. However, in the complex, helix α_1 of RPP21 extends through residues 9–17, indicating that binding is associated with induced fit in RPP21 as well. The RPP29 binding interface of RPP21 is clearly mapped to one face of the helix bundle by the cluster of residues identified with the largest CSPs. Backbone atoms of free and RPP29-bound RPP21 superpose with an overall RMSD of 2.5 Å. However, when superposing the N-terminal helices and C-terminal sheet individually, the agreement is much better, with RMSD of 1.2 and 1.1 Å, respectively, reflecting the relatively poorly defined central linker in free RPP21 and corresponding uncertainty in interdomain orientation.[35] The N-terminal helices of *Pfu* RPP21 that form the binding interface adopt the same overall structure as observed in crystals of the *Pho* RPP21–RPP29 complex, with a backbone RMSD of 0.7 Å.

Interface between RPP29 and RPP21

The structure of the *Pfu* RPP21–RPP29 intermolecular interface identified from CSPs (Fig. 1) was defined by 284 unique intermolecular NOEs, many of which arise between methyl-bearing and aromatic residues (Supporting Information). These NOEs highlight an extensive interface that buries approximately 2400 Å^2 of surface on both proteins (RPP29, 1100 Å^2; RPP21, 1300 Å^2) and is composed of hydrophobic, polar, and ionic interactions between residues provided in three separate structural elements: (1) the N-terminal region of RPP29 extends in an antiparallel fashion along RPP21 helix α_1; (2) RPP29 β2 interacts with both helices of RPP21 in the center of the interface; and (3) the C-terminal helix of RPP29 stabilizes the end of RPP21 helix α_2 (Fig. 4).

In addition to hydrophobic interactions, conserved polar contacts likely play an important role in stabilizing the complex. In an unusual feature, I71^{RPP29} in strand β2 adopts backbone φ/ψ torsion angles (140±3 and −53±12, respectively) that allow side chains of both I71^{RPP29} and D72^{RPP29} to participate in the RPP21 interface, through hydrophobic interactions and an intermolecular salt bridge, respectively. Moreover, this unusual backbone configuration orients the backbone carbonyl of I71^{RPP29} into the interface, where it is available for a stabilizing interaction with the side-chain hydroxyl of Y39^{RPP21}. Although intermolecular NOEs were observed between I71^{RPP29} and Y39^{RPP21} (Supporting Information), these NOEs were not sufficient to constrain the side chain of Y39^{RPP21} such that

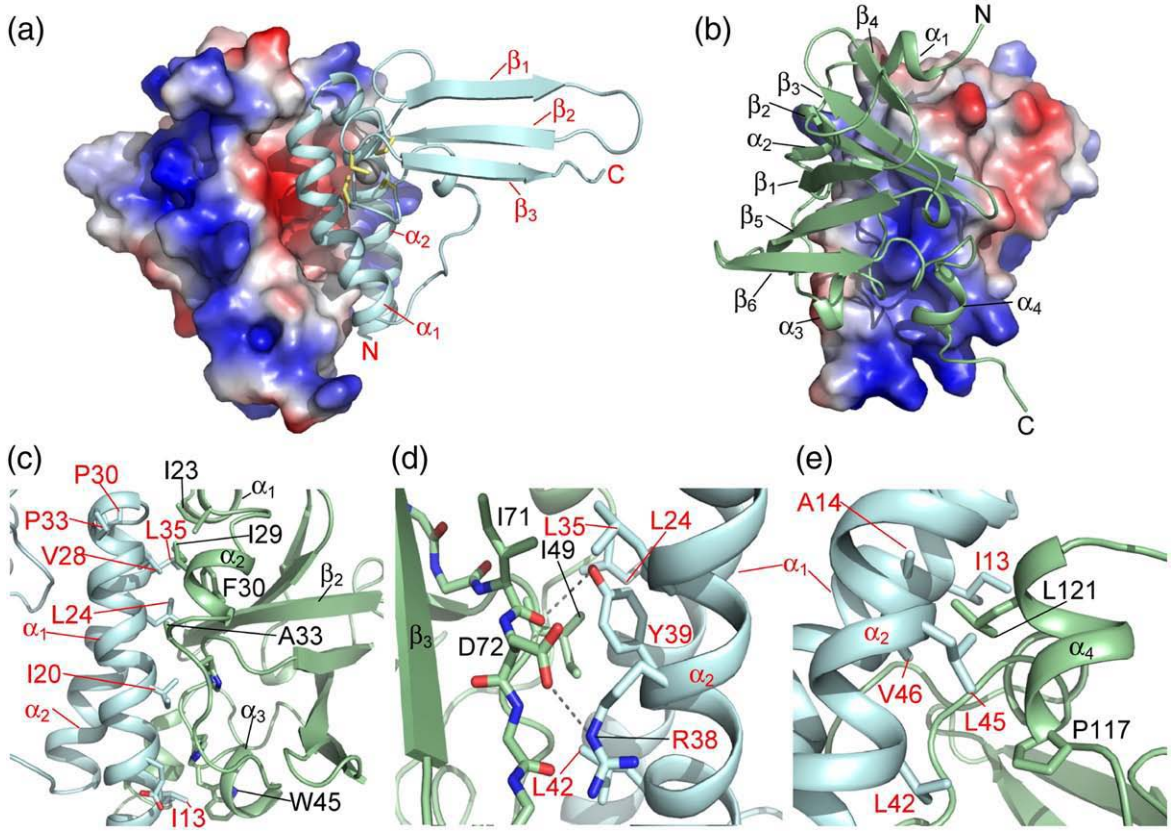

Fig. 4. Interface of the *Pfu* RPP29–RPP21 complex. Electrostatic potential maps on the surface of RPP29 (a) and RPP21 (b) illustrate that the interface is dominated by hydrophobic interactions surrounding prominent charge–charge interactions; the binding partner is shown as a ribbon (RPP21 in cyan and RPP29 in green). (c–e) Close-up showing three elements that stabilize the protein–protein complex. The lowest-energy structure is chosen as the representative. The structure ensemble of these same views are provided in Supporting Information.

I71^{RPP29} O and Y39^{RPP21} O$^{\eta}$ are in hydrogen-bonding distance in each member of the ensemble (3.3±0.4 Å). This interaction was also observed in the crystal structure of the *Pho* RPP21–RPP29 complex,[42] and mutation of Y39^{RPP21} to alanine was shown to be strongly deleterious to activity in an *in vitro* reconstitution assay.[34] Given the sequence conservation in this region of both proteins, this is likely to be a conserved interaction across archaea and eukarya. Adjacent to this interaction, prominent intermolecular salt bridges appear to be formed between E47^{RPP29} and R17^{RPP21} and between D72^{RPP29} and R38^{RPP21} (Fig. 4d). These charge pairs are highly conserved in the thermophilic and hyperthermophilic RPPs in archaea (Supporting Information). Many of the residues in the binding surfaces of both proteins are highly conserved or invariant (Supporting Information), suggesting a conserved binding interface between RPP29 and RPP21 in archaeal and eukaryotic RNase P.

RNA binding surface

RNA binding studies of *Mth* and *Saccharomyces cerevisiae* RPPs using the yeast three-hybrid system showed that RPP29 binds the RPR in *Mth* and yeast RNase P, and both RPP21 and RPP29 interact directly with H1 RNA (RPR) in human RNase P.[40,46] Given that RPP29 and RPP21 form a tight and intimate complex, it is reasonable to imagine that this complex forms prior to assembly with the RPR and, thus, may constitute an RNA binding "unit" with one or more contiguous RNA binding surfaces. The electrostatic potential map of the *Pfu* RPP29–RPP21 complex identifies two surface patches with positive electrostatic potential on difference faces of the complex (Fig. 5). The larger of these two surfaces (site 1) indeed spans both proteins, including the RPP21 central linker and helix α_3 at the N-terminus, as well as β6 and the C-terminal α-helix of RPP29. Twenty highly conserved Arg and Lys residues are located on this surface patch, among them, R116, R120, and K123 in the C-terminal helix of RPP29 and K51, K53, K59, R60, R61, and K64 in the central linker of RPP21. The smaller site 2 is localized to the RPP21 β-sheet, with R77, R79, R81, K83, R84, K91, R100, and two His (H87 and H97), all extending on one face of the β-sheet. Of these, R100 is invariant and R77, R79, R81, and K91 are highly conserved in archaea and eukarya (Supporting Information). This analysis draws attention to two distinct faces of the binary complex as potential RNA binding interfaces for the RPR catalyst and pre-tRNA substrate.

Footprinting

Knowledge of the spatial organization of these RPPs on the cognate RPR is necessary to better understand how the archaeal RPPs support RPR catalysis. We previously employed footprinting assays and demonstrated that the POP5–RPP30 binary complex, and not RPP21–RPP29, decreased the susceptibility to RNase T1 cleavage of a *Pfu* RPR

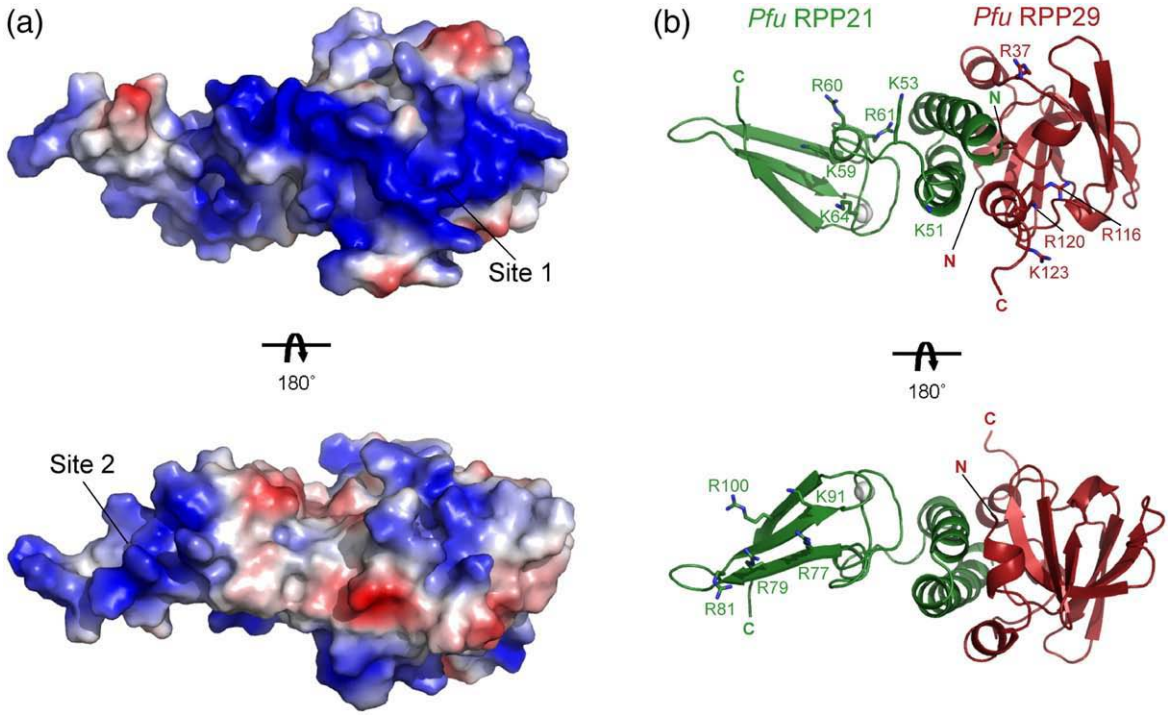

Fig. 5. Electrostatic potential map suggests two RNA binding regions. (a) Electrostatic potential map of the *Pfu* RPP29–RPP21 complex reveals two extended electropositive surface patches. The larger of these surfaces is composed of residues contributed by both proteins; the smaller is localized solely to the RPP21 zinc ribbon. (b) Highly conserved basic residues are shown on the ribbon diagrams of *Pfu* RPP29 (red) and *Pfu* RPP21 (green). The orientation is as in (a).

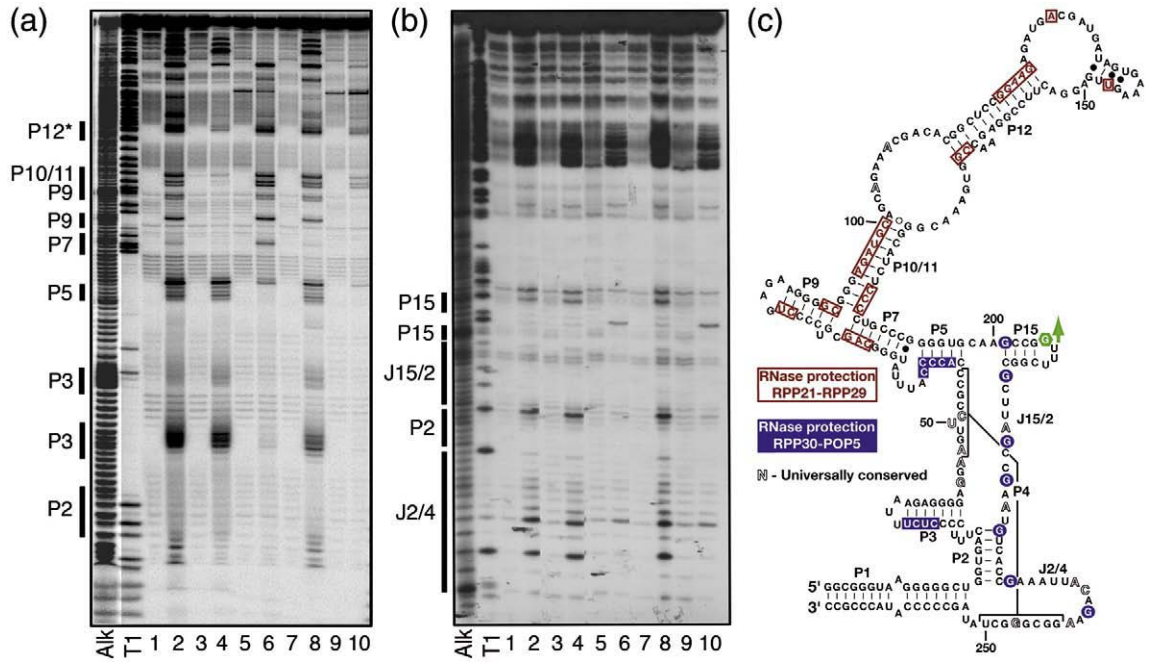

Fig. 6. Footprinting using RNase V1 and RNase T1 to identify RPP-binding sites in *Mja* RPR. *Mja* RPR labeled at the 5′-end (a) or 3′-end (b) was incubated either without (lanes 1, 3, 5, 7, and 9) or with (lanes 2, 4, 6, 8, and 10) RNase V1 (a) or RNase T1 (b). *Mja* RPR was present alone (lanes 1, 2, 7, and 8), with RPP21–RPP29 (lanes 3 and 4), with RPP30–POP5 (lanes 5 and 6), or with both binary complexes (lanes 9 and 10). Since reconstitution of the RPR with each binary RPP complex is performed in a buffer different from that used for reconstitution with both binary complexes together, two different control RNase T1/V1 digestions of the RPR are shown (lanes 1 and 2 for binary RPPs, and lanes 7 and 8 for both binary pairs). "Alk" and "T1" represent molecular size ladders generated by subjecting end-labeled, denatured *Mja* RPRs to alkaline hydrolysis and partial RNase T1 digestion, respectively. The RNase T1 cleavage sites were also mapped by using primer extension assays (data not shown).[29] *Longer electrophoretic runs were used to map protection patterns distal to the labeled termini (see Supporting Information). (c) Summary of the RPP footprinting data depicted on a secondary-structure model of *Mja* RPR. Circled and boxed nucleotides indicate protection to RNase T1 and RNase V1, respectively; blue and red colors indicate regions of protection by RPP30–POP5 and RPP21–RPP29, respectively. The green arrow indicates an RPR position that showed increased susceptibility to RNase T1 in the presence of either RPP30–POP5 or all four RPPs. RNase V1 cleavages around nucleotides 130–150 suggest that the secondary structure as drawn may need to be revised.

deletion derivative containing only the C domain.[13] As documented before, technical problems complicated footprinting experiments with the full-length *Pfu* RPR.[13] Therefore, we explored *Mja* RNase P as an alternative to its *Pfu* relative and were able to map the RPP-binding sites on this shorter RPR. Full-length *Mja* RPR was digested with either RNase T1 (which cleaves 3′ to unpaired guanines) or RNase V1 (which cleaves base-paired nucleotides in RNA). In the presence of the *Mja* RPP29–RPP21 complex, the paired regions P9, P10/11, and P12 in the S domain are protected from V1 cleavage, while no protection by RPP29–RPP21 complex was observed in the C domain (Fig. 6). This observation is also consistent with the finding that addition of RPP21–RPP29 (unlike POP5–RPP30) to the S-domain-deleted *Pfu* and *Mja* RPRs changes neither the rate nor the NH_4^+/Mg^{2+} requirement, unlike its effects on the full-length archaeal RPRs.[13,29] In contrast to RPP21–RPP29, *Mja* RPP30–POP5 protects from RNase T1 cleavage the RPR's C domain, especially at or surrounding the universally conserved nucleotides (Fig. 6). No additional regions of protection were observed when all four RPPs were present compared to the aggregate of the footprints of each binary pair (compare lanes 4, 6, and 10, Fig. 6a and b). Collectively, these footprinting studies indicate that RPP30–POP5 and RPP21–RPP29 exclusively interact with the C and S domains, respectively, regardless of whether the other pair is present. Our ongoing studies with another type A RNase P (*Mth*) reveal a similar binding pattern (data not shown). Considering the conservation of sequence and or secondary structural elements at or near the RPP-binding sites, we can reasonably expect similar RNA–protein interactions in archaeal and eukaryotic RNase P holoenzymes.

Conclusion

The NMR data presented here indicate that formation of the *Pfu* RPP29–RPP21 complex involves binding-coupled folding of structural elements in both proteins. The RPP29–RPP21 complex is defined by a combination of conserved interfacial hydrophobic and polar residues, including apparent salt bridges. Outside of the structured cores, residues in the extreme N- and C-termini of both

proteins indicate that these remain unstructured in the protein complex. Of particular interest are the long N-terminus of RPP29 (17 residues) and the C-terminus of RPP21 (13 residues), both of which possess an abundance of conserved and basic residues (Lys, Arg) that suggest a role in RNA binding. The surface of the protein–protein complex features two well-defined regions of positive electrostatic potential, highlighting possible RNA binding regions.

The structure of the *Pfu* RPP21–RPP29 complex, together with enzymatic footprinting data, permits informed speculation about the nature of the protein–RNA complex. Enzymatic footprinting of *Mja* RPP21–RPP29 on the *Mja* RPR indicates that this protein complex interacts only with the S domain of the RPR, consistent with earlier studies where it was shown to not affect the rate of the phosphodiester bond-breaking step[29] (Fig. 6). Since there is no 3D model of any archaeal RPR presently, the crystal structures of the bacterial RPRs serve as the best frame of reference. The crystal structure of the *T. thermophilus* RPR S domain highlights intramolecular RNA–RNA interactions (especially between stems P13 and P12 and between P14 and P8) that stabilize the tertiary structure necessary for RPR-alone catalysis.[18] However, when compared to the bacterial type A RPR, P13 and P14 are absent from the S domain of *Pfu* and *Mja* RPRs, which instead exhibit an extended P12. It is tempting to propose that in archaeal RNase P, the 3D fold of the RPR is maintained and that the stabilizing RNA–RNA interactions in the bacterial enzyme are replaced by RNA–protein interactions in archaeal RNase P.[47] Thus, given the location of RNA binding by the RPP21–RPP29 complex, the function of this complex might be to compensate for the absence of the P13/P14 structural elements by mediating tertiary contacts between different parts of the RPR.

The presence of a second potential RNA-binding surface localized to the RPP21 β-sheet suggests a function unrelated to stabilizing RPR tertiary structure. Since human RPP21 has been reported to bind precursor tRNA,[48] it is conceivable that archaeal RPP21 might also be involved in substrate recognition. The S domain in bacterial RPR has been shown to recognize the T stem–loop (TSL) region in the ptRNA. The TSL–S domain interaction triggers a conformational change that aids catalysis by positioning the chemical groups and catalytically important Mg^{2+} near the cleavage site in the C domain.[18,49,50] Thus, binding of RPP21–RPP29 to the archaeal RPR's S domain might not only promote intra- and/or interdomain RPR cooperation but also directly (or indirectly via the RPR) mediate recognition of the TSL in the precursor tRNA. Further experimentation is required to evaluate if, indeed, the two potential RNA-binding sites identified in the electrostatic potential map of the RPP21–RPP29 complex play distinctive or overlapping roles in RPR and ptRNA binding.

In summary, we have determined the solution structure of the *Pfu* RPP29–RPP21 complex and found that poorly structured elements in each protein fold to form the intermolecular interface in the complex. Analysis of the electrostatic potential surface of this complex revealed two potential RNA-binding surfaces, the larger of which is composed of surface elements from both proteins. Finally, we have localized the RPP29–RPP21 complex to the S domain of archaeal RPR by enzymatic footprinting. These findings provide valuable new insights into mechanisms of RNP assembly and serve as important steps towards a 3D model of this ancient RNP enzyme.

Materials and Methods

Protein expression and purification

Pfu RPP29

The *Pfu* RPP29/pET-33b plasmid[13] was transformed into *Escherichia coli* BL21(DE3) Rosetta cells (Novagen). The cells were grown in 2-L flasks in a shaker–incubator at 37 °C in LB or minimal M9 media containing 1 g/L of $^{15}NH_4Cl$ and 2 g/L of ^{13}C-glucose as the sole nitrogen and carbon sources, supplemented with 30 μg/L of kanamycin and 34 μg/L of chloramphenicol. Production of the recombinant proteins was induced by addition of 0.5 mM IPTG at an A_{600} of 0.6 and harvested after 4 h by centrifugation. The cell pellet from 1 L of culture was resuspended in 30 mL of buffer *R* (25 mM Tris–HCl, pH 7, 1 mM ethylenediaminetetraacetic acid, 0.1 mM PMSF, and 50 mM DTT), lysed on ice by sonication, and centrifuged (15 min, 8000*g*), and the pellet was resuspended in 30 mL of buffer *R* containing 7 M urea. The solution was sonicated on ice again, and the cell debris was removed by centrifugation (15 min, 8000*g*). The supernatant was filtered (0.45 μm) and loaded onto a 5-mL HiTrap SP column. *Pfu* RPP29 was eluted using a 50-mL linear 10–25% gradient of 25 mM to 2 M KCl under denaturing conditions (25 mM Tris–HCl, pH 7, 0.1 mM PMSF, and 7 M urea), refolded by dialyzing into NMR buffer [10 mM Tris–HCl, pH 6.7, 10 mM KCl, 0.3 mM $ZnCl_2$, and 0.02% (w/v) NaN_3], and concentrated by ultrafiltration with a 5-kDa molecular mass cutoff membrane (Ultra-4, Amicon).

Pfu RPP21

The *Pfu* RPP21 protein was overexpressed and purified as previously described,[35] except that at each refolding step, the protein was refolded from denaturant solutions (8 M urea) by dialysis, instead of by rapid buffer exchange in a size-exclusion column: (1) the protein eluted from the nickel-loaded Hi-Trap chelating column (GE Healthcare) was refolded into NMR buffer by dialysis before thrombin cleavage; (2) the lyophilized protein following HPLC purification was resuspended in denaturing buffer and refolded by dialyzing against NMR buffer.

NMR spectroscopy and resonance assignments

The *Pfu* RPP21–RPP29 complex was formed by combining each U-^{15}N,^{13}C-labeled protein (~1 mM) with an unlabeled protein partner at a 1:1.2 molar ratio to promote full saturation of the labeled protein.[35] Taking advantage of the thermostability of *Pfu* proteins, we

recorded NMR spectra at 55 °C on 600- and 800-MHz Bruker Avance DRX spectrometers (Billerica, MA) equipped with triple-resonance pulse-field gradient probes. NMR spectra were processed and analyzed by NMRPipe,[51] NMRView,[52] and CARA.[53]

Assignments of ^{1}H, ^{15}N, and ^{13}C resonances for each labeled protein in complex with its unlabeled partner were obtained by using data from the following experiments at 600 MHz: ^{15}N–^{1}H HSQC, ^{13}C–^{1}H HSQC, HNCO, HNCACB, CBCA(CO)NH, C(CO)NH-total correlated spectroscopy (τ_m = 12 ms), and H(C)(CO)NH-total correlated spectroscopy (τ_m = 12 ms).[54] Distance restraints were obtained from 3D ^{15}N-separated NOESY-HSQC (τ_m = 100 ms) and ^{13}C-separated NOESY-HSQC (τ_m = 100 ms) spectra recorded at 800 MHz on samples dissolved in 10% and 99.8% D_2O, respectively. Intermolecular distance restraints were assigned initially from ^{13}C-filtered/edited NOESY-HSQC spectra (τ_m = 100 ms, 800 MHz, 99.8% D_2O) with the two $^{1}J_{CH}$ filter elements tuned to 120 and 160 Hz.[43,44]

A heteronuclear $\{^{1}H\}$–^{15}N NOE experiment was recorded at 600 MHz on [U-^{15}N,^{13}C]RPP29 bound to unlabeled RPP21 in an interleaved manner with (NOE) and without (no NOE) ^{1}H saturation.[55] Heteronuclear NOE values were determined from the ratios of the peak intensities between the two spectra.

Structure determination

Distance restraints were derived from the NOE peak intensities, which were calibrated by assigning the median intensity to an interproton distance, r, of 2.7 Å and scaling the remaining intensities by $1/r^6$.[52] Restraints for methyl groups and geminal protons were adjusted by adding 0.5 Å to the upper bound. Backbone torsion-angle restraints were obtained from analysis of the backbone chemical shifts via TALOS.[56] Hydrogen bonds were identified based on the secondary structural information and characteristic NOE patterns.

Structure calculations were performed using simulated annealing protocols within the Xplor-NIH software suite.[57] Preliminary analyses of the ^{15}N,^{13}C-edited and ^{13}C-filtered/edited NOE spectra identified a total of 323 unique (nonredundant) unambiguous NOEs, including 105 intramolecular NOEs in RPP21, 124 intramolecular NOEs in RPP29, and 284 intermolecular NOEs in the binding interface. An initial set of structures of each individual protein was generated using the unique intramolecular NOEs, in addition to short-range NOE restraints and dihedral angle restraints. These initial ensembles (RPP21 and RPP29, respectively) were then used as templates for iterative computer-aided structure-based NOE assignment (SANE, or structure-assisted NOE evaluation)[58] of the isolated proteins, resulting in assignment of additional intramolecular NOEs. Then, using the NOE and dihedral angle restraints obtained for the refined structure ensembles of the individual proteins, and the 284 intermolecular NOEs, an initial ensemble of the protein–protein complex was generated from an extended template. This initial docked ensemble of the complex served as the template for iterative SANE, yielding an additional 191 intermolecular NOEs. One hundred trials of restraint-driven refinement resulted in an ensemble of ~70 structures with similar restraint energies, from which a final set of 10 structures was selected for analysis and evaluation with Xplor-NIH and PROCHECK-NMR.[45] Surface burial was calculated using the program STC.[59]

RNase T1- and RNase V1-based footprinting to map RNA–protein interactions in *Mja* RNase P

Details regarding the purification of RPPs and reconstitution of *Mja* RNase P are described elsewhere.[29,60] The footprinting studies were conducted as follows. Each 40-μL footprinting reaction contained a trace amount of end-labeled (100,000 dpm, ~0.5 nM) and unlabeled (125 nM) RPR either alone or complexed with RPP21–RPP29 or RPP30–POP5 (1.25 μM) in 50 mM Tris–acetate (pH 7.5), 120 mM $Mg(OAc)_2$, and 400 mM $NH_4(OAc)$. For the reactions with all four RPPs, the reconstitution was performed in 50 mM Tris–acetate (pH 7.5), 30 mM $Mg(OAc)_2$, and 800 mM $NH_4(OAc)$. In all cases, the reconstitutions involved two sequential incubations for 10 min at 37 and 55 °C. Subsequently, 1 μL RNase T1 [0.1 U/μL, diluted 10-fold in water from commercial stock (Ambion)] was added to the reconstitution mix and the incubation was continued at 55 °C for an additional 1 min for the RNA-alone reaction and 5 min for the RNP reactions. Alternatively, 1 μL RNase V1 [0.02 U/μL, diluted 5-fold in water from commercial stock (Ambion)] was added to the reconstitution mix and the incubation was continued at 55 °C for an additional 1 min for the RNA-alone reaction and 8 min for the RNP reactions. Both the T1 and V1 reactions were terminated by adding 10 μL of buffer-saturated phenol (pH 8) followed by extraction with phenol/chloroform. The RNAs were precipitated by adding two volumes of ethanol in the presence of 0.3 M sodium acetate (pH 5.2) and 20 μg/mL glycogen. The RNAs were then pelleted at 18,000*g* for 15 min, and the pellets were washed twice with 70% (v/v) ethanol. The air-dried RNA samples were then resuspended in 10 μL loading dye [9 M urea, 0.9 mM ethylenediaminetetraacetic acid, 0.05% (w/v) bromophenol blue, 0.05% (w/v) xylene cyanol, and 10% (v/v) phenol], separated by 8% (w/v) polyacrylamide/7 M urea gel electrophoresis, and visualized by using a Typhoon PhosphorImager (GE Healthcare). Size markers were generated by using both a partial hydrolysis of the RPR in alkali and digestion of the RPR with RNase T1 under denaturing conditions.[13] Compression-related artifacts during denaturing PAGE occasionally skews ladder assignments by a few nucleotides.

In addition to direct mapping of the cleaved fragments, we also employed primer extension assays as a secondary validation.[29,60] After cleavage by RNase T1, the reaction contents were precipitated, washed with 70% (v/v) ethanol, air-dried, and resuspended in water. The oligonucleotide *Mja*RPR-R (5′-GGGGGATCCGTC-TCGGCGGGTATGGGGGC-3′), which is complementary to the 3′-end of *Mja* RPR, was 5′-labeled with [γ-^{32}P]ATP and T4 polynucleotide kinase and used to prime the reverse transcription of the partial digestion products of *Mja* RPR. To minimize artificial stops caused by the secondary structure of the RPR, we performed the extension reactions at 50 °C using ThermoScript (Invitrogen) reverse transcriptase as specified by the supplier. The products of the reverse transcription reactions were separated in an 8% (w/v) polyacrylamide/7 M urea gel in parallel with a DNA sequencing ladder using *Mja*RPR-R as the primer and the plasmid pBT7-*Mja* RPR[29]as the template.

Accession numbers

Coordinates and restraints have been deposited in the Protein Data Bank with accession number 2KI7. NMR resonance assignments have been deposited in the

Biological Magnetic Resonance Data Bank with accession number 16266.

Acknowledgements

We thank C. Yuan and C. Cottrell (Campus Chemical Instrument Center) for assistance with the NMR data collection and R. C. Wilson, I. R. Kleckner, and the members of the V. Gopalan laboratory (especially Lien Lai) for reagents, encouragement, and helpful discussions. This work was supported by a grant from the National Institutes of Health to M.P.F and V.G. (GM067807).

Supplementary Data

Supplementary data associated with this article can be found, in the online version, at doi:10.1016/j.jmb.2009.08.068

References

1. Altman, S. (2007). A view of RNase P. *Mol. Biosyst.* **3**, 604–607.
2. Gopalan, V. & Altman, S. (2006). Ribonuclease P: structure and catalysis. In *The RNA World* (Gesteland, R., Cech, T. & Atkins, J., eds), Cold Spring Harbor Laboratory Press, Cold Spring Harbor, NY; (only online at http://rna.cshl.edu).
3. Evans, D., Marquez, S. M. & Pace, N. R. (2006). RNase P: interface of the RNA and protein worlds. *Trends Biochem. Sci.* **31**, 333–341.
4. Guerrier-Takada, C., Gardiner, K., Marsh, T., Pace, N. & Altman, S. (1983). The RNA moiety of ribonuclease P is the catalytic subunit of the enzyme. *Cell*, **35**, 849–857.
5. Pannucci, J. A., Haas, E. S., Hall, T. A., Harris, J. K. & Brown, J. W. (1999). RNase P RNAs from some Archaea are catalytically active. *Proc. Natl Acad. Sci. USA*, **96**, 7803–7808.
6. Kikovska, E., Svard, S. G. & Kirsebom, L. A. (2007). Eukaryotic RNase P RNA mediates cleavage in the absence of protein. *Proc. Natl Acad. Sci. USA*, **104**, 2062–2067.
7. Hsieh, J., Andrews, A. J. & Fierke, C. A. (2004). Roles of protein subunits in RNA–protein complexes: lessons from ribonuclease P. *Biopolymers*, **73**, 79–89.
8. Sun, L., Campbell, F. E., Zahler, N. H. & Harris, M. E. (2006). Evidence that substrate-specific effects of C5 protein lead to uniformity in binding and catalysis by RNase P. *EMBO J.* **25**, 3998–4007.
9. Sun, L. & Harris, M. E. (2007). Evidence that binding of C5 protein to P RNA enhances ribozyme catalysis by influencing active site metal ion affinity. *RNA*, **13**, 1505–1515.
10. Smith, J. K., Hsieh, J. & Fierke, C. A. (2007). Importance of RNA–protein interactions in bacterial ribonuclease P structure and catalysis. *Biopolymers*, **87**, 329–338.
11. Hartmann, E. & Hartmann, R. K. (2003). The enigma of ribonuclease P evolution. *Trends Genet.* **19**, 561–569.
12. Gopalan, V. (2007). Uniformity amid diversity in RNase P. *Proc. Natl Acad. Sci. USA*, **104**, 2031–2032.
13. Tsai, H. Y., Pulukkunat, D. K., Woznick, W. K. & Gopalan, V. (2006). Functional reconstitution and characterization of *Pyrococcus furiosus* RNase P. *Proc. Natl Acad. Sci. USA*, **103**, 16147–16152.
14. Hall, T. A. & Brown, J. W. (2002). Archaeal RNase P has multiple protein subunits homologous to eukaryotic nuclear RNase P proteins. *RNA*, **8**, 296–306.
15. Kazantsev, A. V. & Pace, N. R. (2006). Bacterial RNase P: a new view of an ancient enzyme. *Nat. Rev., Microbiol.* **4**, 729–740.
16. Brown, J. W. (1999). The Ribonuclease P Database. *Nucleic Acids Res.* **27**, 314.
17. Loria, A. & Pan, T. (1996). Domain structure of the ribozyme from eubacterial ribonuclease P. *RNA*, **2**, 551–563.
18. Krasilnikov, A. S., Xiao, Y., Pan, T. & Mondragon, A. (2004). Basis for structural diversity in homologous RNAs. *Science*, **306**, 104–107.
19. Krasilnikov, A. S., Yang, X., Pan, T. & Mondragon, A. (2003). Crystal structure of the specificity domain of ribonuclease P. *Nature*, **421**, 760–764.
20. Torres-Larios, A., Swinger, K. K., Krasilnikov, A. S., Pan, T. & Mondragon, A. (2005). Crystal structure of the RNA component of bacterial ribonuclease P. *Nature*, **437**, 584–587.
21. Kazantsev, A. V., Krivenko, A. A., Harrington, D. J., Holbrook, S. R., Adams, P. D. & Pace, N. R. (2005). Crystal structure of a bacterial ribonuclease P RNA. *Proc. Natl Acad. Sci. USA*, **102**, 13392–13397.
22. Kazantsev, A. V., Krivenko, A. A., Harrington, D. J., Carter, R. J., Holbrook, S. R., Adams, P. D. & Pace, N. R. (2003). High-resolution structure of RNase P protein from *Thermotoga maritima*. *Proc. Natl Acad. Sci. USA*, **100**, 7497–7502.
23. Stams, T., Niranjanakumari, S., Fierke, C. A. & Christianson, D. W. (1998). Ribonuclease P protein structure: evolutionary origins in the translational apparatus. *Science*, **280**, 752–755.
24. Spitzfaden, C., Nicholson, N., Jones, J. J., Guth, S., Lehr, R., Prescott, C. D. *et al.* (2000). The structure of ribonuclease P protein from *Staphylococcus aureus* reveals a unique binding site for single-stranded RNA. *J. Mol. Biol.* **295**, 105–115.
25. Tsai, H. Y., Masquida, B., Biswas, R., Westhof, E. & Gopalan, V. (2003). Molecular modeling of the three-dimensional structure of the bacterial RNase P holoenzyme. *J. Mol. Biol.* **325**, 661–675.
26. Buck, A. H., Kazantsev, A. V., Dalby, A. B. & Pace, N. R. (2005). Structural perspective on the activation of RNase P RNA by protein. *Nat. Struct. Mol. Biol.* **12**, 958–964.
27. Niranjanakumari, S., Day-Storms, J. J., Ahmed, M., Hsieh, J., Zahler, N. H., Venters, R. A. & Fierke, C. A. (2007). Probing the architecture of the *B. subtilis* RNase P holoenzyme active site by cross-linking and affinity cleavage. *RNA*, **13**, 521–535.
28. Harris, J. K., Haas, E. S., Williams, D., Frank, D. N. & Brown, J. W. (2001). New insight into RNase P RNA structure from comparative analysis of the archaeal RNA. *RNA*, **7**, 220–232.
29. Pulukkunat, D. K. & Gopalan, V. (2008). Studies on *Methanocaldococcus jannaschii* RNase P reveal insights into the roles of RNA and protein cofactors in RNase P catalysis. *Nucleic Acids Res.* **36**, 4172–4180.
30. Boomershine, W. P., McElroy, C. A., Tsai, H. Y., Wilson, R. C., Gopalan, V. & Foster, M. P. (2003). Structure of Mth11/Mth Rpp29, an essential protein

subunit of archaeal and eukaryotic RNase P. *Proc. Natl Acad. Sci. USA*, **100**, 15398–15403.
31. Sidote, D. J. & Hoffman, D. W. (2003). NMR structure of an archaeal homologue of ribonuclease P protein Rpp29. *Biochemistry*, **42**, 13541–13550.
32. Sidote, D. J., Heideker, J. & Hoffman, D. W. (2004). Crystal structure of archaeal ribonuclease P protein aRpp29 from *Archaeoglobus fulgidus*. *Biochemistry*, **43**, 14128–14138.
33. Numata, T., Ishimatsu, I., Kakuta, Y., Tanaka, I. & Kimura, M. (2004). Crystal structure of archaeal ribonuclease P protein Ph1771p from *Pyrococcus horikoshii* OT3: an archaeal homolog of eukaryotic ribonuclease P protein Rpp29. *RNA*, **10**, 1423–1432.
34. Kakuta, Y., Ishimatsu, I., Numata, T., Kimura, K., Yao, M., Tanaka, I. & Kimura, M. (2005). Crystal structure of a ribonuclease P protein Ph1601p from *Pyrococcus horikoshii* OT3: an archaeal homologue of human nuclear ribonuclease P protein Rpp21. *Biochemistry*, **44**, 12086–12093.
35. Amero, C. D., Boomershine, W. P., Xu, Y. & Foster, M. (2008). Solution structure of *Pyrococcus furiosus* RPP21, a component of the archaeal RNase P holoenzyme, and interactions with its RPP29 protein partner. *Biochemistry*, **47**, 11704–11710.
36. Wilson, R. C., Bohlen, C. J., Foster, M. P. & Bell, C. E. (2006). Structure of Pfu Pop5, an archaeal RNase P protein. *Proc. Natl Acad. Sci. USA*, **103**, 873–878.
37. Takagi, H., Watanabe, M., Kakuta, Y., Kamachi, R., Numata, T., Tanaka, I. & Kimura, M. (2004). Crystal structure of the ribonuclease P protein Ph1877p from hyperthermophilic archaeon *Pyrococcus horikoshii* OT3. *Biochem. Biophys. Res. Commun.* **319**, 787–794.
38. Kifusa, M., Fukuhara, H., Hayashi, T. & Kimura, M. (2005). Protein–protein interactions in the subunits of ribonuclease P in the hyperthermophilic archaeon *Pyrococcus horikoshii* OT3. *Biosci. Biotechnol. Biochem.* **69**, 1209–1212.
39. Hall, T. A. & Brown, J. W. (2004). Interactions between RNase P protein subunits in archaea. *Archaea*, **1**, 247–254.
40. Houser-Scott, F., Xiao, S., Millikin, C. E., Zengel, J. M., Lindahl, L. & Engelke, D. R. (2002). Interactions among the protein and RNA subunits of *Saccharomyces cerevisiae* nuclear RNase P. *Proc. Natl Acad. Sci. USA*, **99**, 2684–2689.
41. Kawano, S., Nakashima, T., Kakuta, Y., Tanaka, I. & Kimura, M. (2006). Crystal structure of protein Ph1481p in complex with protein Ph1877p of archaeal RNase P from *Pyrococcus horikoshii* OT3: implication of dimer formation of the holoenzyme. *J. Mol. Biol.* **357**, 583–591.
42. Honda, T., Kakuta, Y., Kimura, K., Saho, J. & Kimura, M. (2008). Structure of an archaeal homolog of the human protein complex Rpp21–Rpp29 that is a key core component for the assembly of active ribonuclease P. *J. Mol. Biol.* **384**, 652–662.
43. Breeze, A. (2000). Isotope-filtered NMR methods for the study of biomolecular structure and interactions. *Prog. Nucl. Magn. Reson. Spectrosc.* **36**, 323–372.
44. Zwahlen, C, Legault, P., Vincent, S. J. F., Greenblatt, J., Konrat, R. & Kay, L. E. (1997). Methods for measurement of intermolecular NOEs by multinuclear NMR spectroscopy: application to a bacteriophage λ N-peptide/boxB RNA complex. *J. Am. Chem. Soc.* **119**, 6711–6721.
45. Laskowski, R. A., Rullmannn, J. A., MacArthur, M. W., Kaptein, R. & Thornton, J. M. (1996). AQUA and PROCHECK-NMR: programs for checking the quality of protein structures solved by NMR. *J. Biomol. NMR*, **8**, 477–486.
46. Jiang, T., Guerrier-Takada, C. & Altman, S. (2001). Protein–RNA interactions in the subunits of human nuclear RNase P. *Proc. Natl Acad. Sci. USA*, **7**, 937–941.
47. Gopalan, V. (2007). Uniformity amid diversity in RNase P. *Proc. Natl Acad. Sci. USA*, **104**, 2031–2032.
48. Jarrous, N., Reiner, R., Wesolowski, D., Mann, H., Guerrier-Takada, C. & Altman, S. (2001). Function and subnuclear distribution of Rpp21, a protein subunit of the human ribonucleoprotein ribonuclease P. *RNA*, **7**, 1153–1164.
49. Brannvall, M., Kikovska, E., Wu, S. & Kirsebom, L. A. (2007). Evidence for induced fit in bacterial RNase P RNA-mediated cleavage. *J. Mol. Biol.* **372**, 1149–1164.
50. Pan, T., Loria, A. & Zhong, K. (1995). Probing of tertiary interactions in RNA: 2′-hydroxyl-base contacts between the RNase P RNA and pre-tRNA. *Proc. Natl Acad. Sci. USA*, **92**, 12510–12514.
51. Delaglio, F., Grzesiek, S., Vuister, G. W., Zhu, G., Pfeifer, J. & Bax, A. (1995). NMRPipe: a multidimensional spectral processing system based on UNIX pipes. *J. Biomol. NMR*, **6**, 277–293.
52. Johnson, B. A. (2004). Using NMRView to visualize and analyze the NMR spectra of macromolecules. *Methods Mol. Biol.* **278**, 313–352.
53. Keller, R. (2004). The Computer Aided Resonance Assignment Tutorial.
54. Cavanagh, J., Fairbrother, W. J., Palmer, A. G., Skelton, N. J. & Rance, M. (2006). *Protein NMR Spectroscopy: Principles and Practice*, 2nd edit. Academic Press, New York, NY.
55. Kay, L. E., Torchia, D. A. & Bax, A. (1989). Backbone dynamics of proteins as studied by nitrogen-15 inverse detected heteronuclear NMR spectroscopy: application to staphylococcal nuclease. *Biochemistry*, **28**, 8972–8979.
56. Cornilescu, G., Delaglio, F. & Bax, A. (1999). Protein backbone angle restraints from searching a database for chemical shift and sequence homology. *J. Biomol. NMR*, **13**, 289–302.
57. Schwieters, C. D., Kuszewski, J. J., Tjandra, N. & Clore, G. M. (2003). The Xplor-NIH NMR molecular structure determination package. *J. Magn. Reson.* **160**, 65–73.
58. Duggan, B. M., Legge, G. B., Dyson, H. J. & Wright, P. E. (2001). SANE (Structure Assisted NOE Evaluation): an automated model-based approach for NOE assignment. *J. Biomol. NMR*, **19**, 321–329.
59. Lavigne, P., Bagu, J. R., Boyko, R., Willard, L., Holmes, C. F. & Sykes, B. D. (2000). Structure-based thermodynamic analysis of the dissociation of protein phosphatase-1 catalytic subunit and microcystin–LR docked complexes. *Protein Sci.* **9**, 252–264.
60. Pulukkunat, D. K. (2008). Ph. D. Thesis, The Ohio State University, Columbus, OH.